

Large Eddy Simulations of Wake Flows Around a Floating Offshore Wind Turbine Under Complex Atmospheric Inflows

Shun Xu*

Computational Marine Hydrodynamics Lab, School of Naval Architecture, Ocean and Civil Engineering
Shanghai Jiao Tong University, Shanghai, China

Nina Wang and Tiegang Zhuang

Key Laboratory of Far-Shore Wind Power Technology of Zhejiang Province
Huadong Engineering Corporation Limited, Hangzhou, China

Weiwen Zhao* and Decheng Wan*†

Computational Marine Hydrodynamics Lab, School of Naval Architecture, Ocean and Civil Engineering
Shanghai Jiao Tong University, Shanghai, China

This study performed numerical investigations of a floating offshore wind turbine under a complex atmospheric boundary layer inflow. The complex and realistic ABL inflow was generated by large eddy simulations, and wind turbine blades were modeled by the actuator line model. The platform motions were solved by potential theory. A baseline case with a uniform inflow condition was conducted to provide some comparable data. The difference of the aerodynamic power in the two inflow scenarios is minor, except that small bumps in the atmospheric scenario are observed. The yaw moment is significantly enhanced as a result of the lateral asymmetry of the atmospheric inflow on the rotor plane. A significant observation of this study is the large-scale wake meandering caused by the presence of atmospheric turbulence structures. In addition, the high-velocity atmospheric airflow enters in the wind turbine wakes, and its mixing with the low-velocity wakes leads to a faster wake recovery.

INTRODUCTION

In recent years, with the great development of society, traditional fossil resources have had difficulty meeting the significant energy demands. Wind energy harvesting has received increasing attention because wind is a nonpolluting, renewable resource (Chehouri et al., 2015), and the increase in harvesting is responsible for the promising growth of wind turbine technology. According to the 2021 Global Wind Energy Report (Global Wind Energy Council, 2021), the installed capacity of wind turbines in 2020 reached up to 93 GW, resulting in a 53% year-on-year increase. The development trend of wind turbines has gradually moved toward the large-scale and floating type (Asim et al., 2022), which has had significant impacts on the aerodynamic performance and fatigue loads of wind turbines subjected to the complex atmospheric boundary layer (ABL). Consequently, it has become very necessary to study the dynamic responses of a floating offshore wind turbine (FOWT) under a complex ABL inflow.

The effects of the complex ABL inflow on the bottom-fixed wind turbine have been widely researched. By incorporating the large eddy simulations (LES) and actuator line model (ALM), Churchfield, Lee, Michalakes, and Moriarty (2012) presented a numerical study of atmospheric and turbine wakes on wind turbine dynamics. Their findings revealed that the turbulence struc-

tures generated in the ABL can cause the isolated loading events as significant as when a wind turbine is waked by an upstream turbine. Lee et al. (2012) investigated the effects of atmospheric stability and surface roughness on wind turbine fatigue loads; the results showed that the two parameters have significant impacts on turbine fatigue loads. Ning and Wan (2019) examined the wake meandering and its effects on wind turbulence aerodynamics. Liu et al. (2022) studied the wake dynamics of a waked wind turbine with four different downwind spacings and three different inflows. In contrast to the above studies of flat terrain, Li et al. (2022) studied the effects of ground roughness and atmospheric stratification on the wake characteristics of wind turbines over complex terrains. It was found that the effects of the two parameters are superimposed or counteracted, depending on the shape of the complex terrain.

Compared with the bottom-fixed wind turbine, the inflow wind conditions are more simplified on the FOWT because of the complex feature of the two-phase flow. Cheng et al. (2019) performed the fully coupled aerohydrodynamic responses of a FOWT with the combined uniform wind inflow and regular incident wave. To consider the properties of ABL inflow, a simplified shear wind inflow (Huang and Wan, 2019; Huang et al., 2019) was adopted for the FOWT. However, the wind turbine aerodynamic performance is significantly affected by the complex ABL inflow as a result of the large-scale development of wind turbine blades. By generating the ABL wind field based on the Kaimal turbulence model (Kaimal et al., 1972), Li et al. (2018) studied the effects of wind fields on the FOWT aerodynamic performance. Turbulence structures in the ABL wind fields allowed for the observation of the unstable thrust force and power generation. Similarly, Zhou et al. (2022) investigated the aerodynamics and hydrodynamics of a FOWT under different inflow wind conditions, and the ABL

*ISOPE Member; †Corresponding author.

Received August 3, 2022; updated and further revised manuscript received by the editors November 4, 2022. The original version (prior to the final updated and revised manuscript) was presented at the Thirty-second International Ocean and Polar Engineering Conference (ISOPE-2022), Shanghai, China (virtual), June 5–10, 2022.

KEY WORDS: Floating offshore wind turbine, atmospheric boundary layer, large eddy simulations, actuator line model, wind turbine wakes.

wind field was generated by the Mann turbulence model (Mann, 1994). However, the Mann and Kaimal turbulence models were originally developed by small-scale onshore wind turbines; the applicability of the two models for ABL wind field generation of large-scale FOWT remains questionable. Consequently, the LES is recommended by the International Electrotechnical Commission as an additional wind turbulence model (Nybø et al., 2022). Johlas et al. (2019, 2020) examined the turbine wake characteristics of FOWT in a complex ABL inflow generated by the LES; in addition, the effects of different platforms on wake characteristics and platform motions were also analyzed.

In this study, numerical simulations of a FOWT subjected to the complex ABL were performed to investigate the dynamic responses and wake characteristics of the FOWT. To generate the quasi-equilibrium ABL flow, the LES with sufficient simulation time was employed. The wind turbine was parameterized by the ALM and the hydrodynamics solved based on the potential theory. In addition, a case of uniform inflow was presented as the reference for the dynamic responses of the FOWT.

NUMERICAL METHODS

Actuator Line Model

The wind turbine blades were modeled based on the ALM, in which the blade surface boundary layer was not resolved. The expensive computational costs were not required, and the satisfied numerical results were also guaranteed by solving the Navier–Stokes equations of flow fields when compared with the blade-resolved method. This ALM was first proposed by Sorensen and Shen (2002); the basic idea behind it is to employ actuator points representing the radial discretized wind turbine blades. The body force of each actuator point is calculated based on the blade element method, and then the body force reacts on flow fields to reflect the influence of wind turbine blades on the flow fields. The body force of actuator point can be expressed by

$$f = (L, D) = \frac{1}{2} \rho U_{\text{rel}}^2 c dr (C_L \vec{e}_L + C_D \vec{e}_D) \quad (1)$$

where L and D are the lift and drag forces of blade element located at the blade radius r , respectively; ρ denotes the air density; U_{rel} represents the relative inflow velocity; c is the chord length of two-dimensional airfoil; dr is the width of blade element; C_L and C_D denote the lift and drag coefficients, respectively; and \vec{e}_L and \vec{e}_D are, in turn, the unit vectors of lift and drag force directions.

Figure 1 shows the velocity vectors of the two-dimensional blade element airfoil; the relative inflow velocity U_{rel} can be obtained by the following formulation.

$$U_{\text{rel}} = \sqrt{U_z^2 + (\Omega r - U_\theta)^2} \quad (2)$$

Inflow angle ϕ is determined by the inflow wind conditions; the local attack angle α is equal to the difference of inflow angle ϕ and local pitch angle γ . Besides this, the added inflow velocity induced by the platform motions should be considered when modeling the FOWT blades.

The body force directly reacting on the flow fields will produce the numerical singularity. Therefore, the Gauss kernel function is adopted on the projection of body force to flow fields. Smoothed body force projection can be calculated by

$$f_\varepsilon = f \otimes \eta_\varepsilon = \sum_{i=1}^N f_i(x_i, y_i, z_i, t) \frac{1}{\varepsilon^3 \pi^{3/2}} \exp\left[-\left(\frac{d_i}{\varepsilon}\right)^2\right] \quad (3)$$

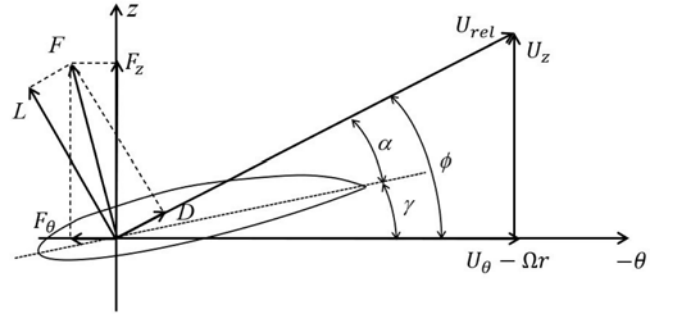


Fig. 1 Velocity vectors of two-dimensional airfoil

where N is the number of actuator points; (x_i, y_i, z_i) denotes the position of i th actuator point; d_i is the distance between the actuator point and projection point; ε is the projection width, where $\varepsilon \approx 2\Delta x$ (Troldborg, 2009) to guarantee numerical stability; and Δx represents the mesh scale around the wind turbine blades.

Governing Equations

The LES was combined with the ALM to study the aerodynamic performance of wind turbine blades. The spatial flited governing equations can be expressed as follows:

$$\begin{aligned} \frac{\partial \bar{u}_i}{\partial x_i} &= 0 \quad (4) \\ \frac{\partial \bar{u}_i}{\partial t} + \frac{\partial}{\partial x_j} (\bar{u}_j \bar{u}_i) &= - \underbrace{\frac{\partial \hat{p}}{\partial x_i}}_{\text{I}} - \underbrace{\frac{1}{\rho_0} \frac{\partial}{\partial x_i} \bar{p}_0(x, y)}_{\text{II}} \\ &\quad - \underbrace{2\varepsilon_{ijk} \Omega_3 \bar{u}_k}_{\text{III}} - \underbrace{\frac{\partial}{\partial x_j} (\tau_{ij}^D)}_{\text{IV}} + \underbrace{\frac{1}{\rho_0} f_i^T}_{\text{V}} \quad (5) \end{aligned}$$

where term I on the right side of momentum equation is the modified pressure gradient; term II is the background pressure gradient to overcome the bottom surface roughness and drive the generation of ABL inflow; term III is the Coriolis force, representing the impact of earth rotation on ABL flow fields; term IV is the tensor of fluid stress, which is calculated by the Smagorinsky sub-scale model (Smagorinsky, 1963); and term V is the body force of wind turbine blades, needed when the wind turbine subjected to the ABL inflow. It is noteworthy that the viscous stress is ignored as a result of the high Reynolds-number nature of the ABL flow. More details about the governing equations can be found in the literature (Churchfield, Lee, Michalakes, and Moriarty, 2012).

Simulation Procedure

The simulation procedure of the FOWT subjected to the ABL inflow is illustrated in Fig. 2. The precursor stage of LES with an 18,800 s simulation time is utilized to simulate the ABL wind field. Specifically, the first 18,000 s are used to generate the quasi-equilibrium flow, which is identified when the velocity sampled at half the boundary layer height oscillates around some mean value. The plane data of upstream boundary are saved as the inflow conditions of the simulations of the FOWT. In the successor stage, the wind turbine is parameterized by the ALM, and the wakes are simulated. The dynamic responses of the FOWT are solved by the FAST code (Jonkman and Buhl, 2005), which is an aero-hydro-servo coupled simulation code for the wind turbine. The blade-pitch controller and the variable-torque controller are employed to regulate the power generation. Note that this simulation procedure

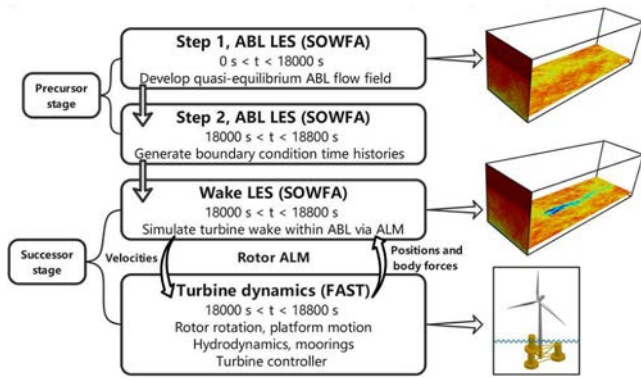


Fig. 2 Simulation procedure of the FOWT under ABL inflow

is carried out under the SOWFA framework (Churchfield, Lee, and Moriarty, 2012), which is an LES solver for the wind farm simulations developed by the National Renewable Energy Laboratory (NREL) based on the OpenFOAM CFD toolbox (OpenFOAM Foundation, 2022). In addition, the two-way coupling with FAST is implemented and available in the SOWFA, and it has been used for investigations of the FOWT under the ABL inflow (Johlas, 2021; Chanprasert et al., 2022). In detail, the wind velocities of the two-dimensional blade elements are sampled in the LES flow field and delivered to FAST. Then the dynamic responses are solved by FAST, and the updated positions and body forces of the wind turbine are delivered to the LES framework. Note that the body forces of the two-dimensional blade elements are determined by the blade element theory (see Fig. 1); the momentum part of the blade element momentum theory is replaced by the ALM.

COMPUTATION SETUP

Model Description

The wind turbine used is the NREL 5MW baseline wind turbine (Jonkman et al., 2009), which is a traditional three-blade wind turbine incorporating a variable-speed torque controller and a blade pitch controller to regulate the power generation based on the operational state. Table 1 shows the main parameters of the wind turbine.

The OC4 DeepCwind semisubmersible platform (Robertson et al., 2014) is used to carry the wind turbine. The platform is made up of three main offset columns inducing buoyance and restoring force, one central column supporting the wind turbine, as well as a series of diagonal cross and horizontal bracing components. Three mooring lines oriented symmetrically are applied to limit floating platform displacements. The relevant properties of floating platform and mooring system are outlined in Table 2.

ABL Inflow

The precursor-successor strategy is employed for the numerical simulations of FOWT’s wakes and dynamics with the condition

Term	Value
Rated power	5 MW
Rated wind velocity	11.4 m/s
Rated rotor velocity	12.1 rpm
Hub height	90 m
Blade number	3

Table 1 Main parameters of NREL 5MW wind turbine

Term	Value
Draft	20 m
Platform mass	13,473,000 kg
Displacement	13,986.8 m ³
Center of mass	(0 m, 0 m, -13.5 m)
Platform roll inertia	6.827 × 10 ⁹ kg · m ²
Platform pitch inertia	6.827 × 10 ⁹ kg · m ²
Platform yaw inertia	1.226 × 10 ¹⁰ kg · m ²
Depth to anchor	200 m
Depth to fairlead	14 m
Mooring line diameter	0.0766 m
Equivalent line mass density	113.35 kg/m
Equivalent mooring line extensional stiffness	753.6 MN

Table 2 Properties of floating platform and mooring system

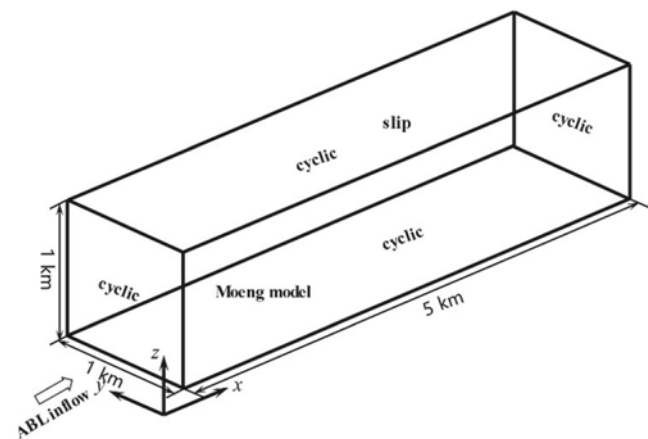


Fig. 3 Calculation region of precursor stage

of ABL inflow. In the precursor stage, the complex ABL inflow is generated in a long-term simulation process. As illustrated in Fig. 3, the periodic boundary conditions are used on the four side walls of the computational region, with the aim of saving computational costs by inducing the size of calculation domain. The top of computational domain is set as the slip boundary condition, indicating that there is no vertical velocity gradient in this plane. The bottom boundary adopts the Moeng wall function model (Moeng, 1984) to calculate the wall shear stress, in which the surface roughness is set to 0.001, representing the typical offshore condition. The length, width, and height of the calculation region are 5,000 m, 1,000 m, and 1,000 m, respectively. And the grid resolution in three directions is 10 m × 10 m × 10 m, corresponding to 5 million grids. Wind velocity and wind direction at the hub height are set to 11.4 m/s and 270°, respectively (along with the x axis).

The numerical simulation time is 18,800 s for the precursor stage, and the first 18,000 s are used to generate the quasi-equilibrium state atmospheric turbulence. The time step is set to 0.4 s to restrict the flow field from advancing more than one grid in a time step. The inflow data in the last 800 s are saved as the input conditions of the successor stage.

In the successor stage, the FOWT is subjected to the complex ABL inflow. The upstream and downstream boundary conditions are modified compared with those of the precursor stage. On the upstream boundary, the velocity is specified using the time- and space-varying boundary condition from the save plane data of the precursor stage. On the downstream boundary, the velocity gra-

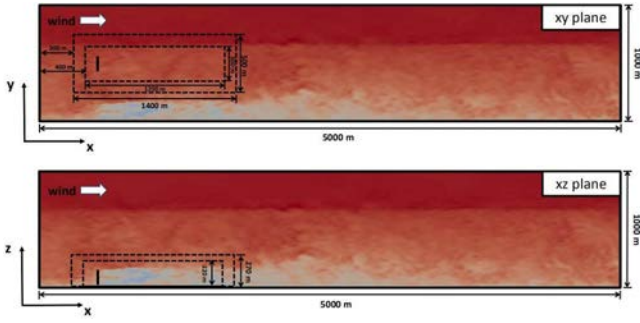


Fig. 4 Mesh refinement configuration of successor stage

dient is set to 0. Figure 4 illustrates the meshing strategy of the successor stage. The wind turbine is located downstream 500 m of the upper inflow boundary. The properties of background mesh are the same as the precursor stage, corresponding to the $10 \text{ m} \times 10 \text{ m} \times 10 \text{ m}$ mesh resolution. A two-level mesh refinement strategy is used around the wind turbine domain to accurately capture the details of wind turbine wakes. The properties of the first and second mesh refinement areas are $1,400 \text{ m} \times 500 \text{ m} \times 270 \text{ m}$ and $1,200 \text{ m} \times 300 \text{ m} \times 220 \text{ m}$ in the x , y , and z directions, respectively, and the distances between the wind turbine and the first and second mesh refinement areas' upstream boundaries are 200 m and 100 m, respectively. The mesh number after refinement is 10.8 million. More details about the mesh refinement can be found in the literature (Cheng et al., 2019; Huang and Wan, 2019; Huang et al., 2019). For the successor stage, the simulation time is 800 s, and the time step is 0.02 s to restrict the blade tip from advancing through more than one grid cell per time step. The simulations are performed on the high-performance computing (HPC) platform of Computational Marine Hydrodynamics Lab (CMHL) at Shanghai Jiao Tong University. The processors of each node are $2 \times$ Intel Xeon Gold 5120 (14 cores, 2.20 GHz) with 128 GB memory and two nodes used. The CPU times for the generation of ABL and the simulation of the FOWT immersed in it are 163 h and 398 h, respectively.

Uniform Inflow

A baseline case of uniform inflow is presented with the purpose of providing some reference data. Note that the Coriolis force is not taken into consideration, and the background pressure gradient is also not needed. Figure 5 shows the mesh refinement strategy of the uniform inflow case for the FOWT. The size of the calculation domain is $1,260 \text{ m} \times 378 \text{ m} \times 378 \text{ m}$ in three direc-

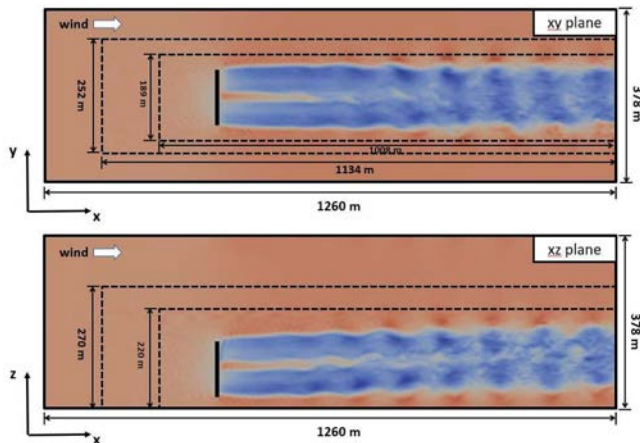


Fig. 5 Mesh refinement configuration of uniform inflow case

tions, and the turbine is located downstream 378 m of the upper inflow boundary. The refined mesh resolution around the wind turbine is the same as that of ABL inflow case, and the resulting mesh number is about 3 million. For the boundary conditions, the upstream boundary is the wind velocity inlet boundary condition, corresponding to a uniform inflow with a 11.4 m/s wind velocity and 270° inflow wind direction. The velocity gradient of downstream boundary is set to 0, and the four side walls are periodic boundary conditions. The simulation time and time step are 800 s and 0.02 s, respectively. One computing node of the HPC platform is used, and the CPU time is 83 h.

Inflow Conditions for the Floating Wind Turbine

As previously mentioned, two different inflow wind conditions, a neutral boundary layer (NBL) complex inflow and uniform wind inflow, are used for the FOWT simulations. The wind velocities for both conditions are 11.4 m/s at hub height. For incident waves, the Stokes first-order deep water wave is applied for both numerical cases, in which the wave height and period are 7.58 m and 12.1 s, respectively. Table 3 shows the inflow conditions of the FOWT; note that the heading angles of wind and wave are both along the x axis.

RESULTS AND DISCUSSION

Simulated Atmospheric Inflow

The time-averaged wind velocity profile and the turbulence intensity in three directions are illustrated in Fig. 6. Note that the turbulence intensity is defined as

$$TI_i(z) = \frac{\sqrt{(U_i(z) - \bar{U}_i(z))^2}}{U_0} \quad (6)$$

where the overbar denotes time average, $U_i(z)$ is the wind velocity of the height of z ($i = x, y, z$), and U_0 is the rated wind velocity of 11.4 m/s. The wind shear is reproduced such that the wind velocity increases with height as a result of the friction on the bottom surface. The wind velocity profile satisfies the logarithmic law, and the wind velocity of hub height is 11.4 m/s, indicating that the desired atmosphere inflow is reproduced. In contrast to the wind velocity, the turbulence intensity decreases with the height. The turbulence intensity in the x -axis direction is more significant than that of the other two directions. Specifically, the turbulence intensity of the hub height is 5.78 in the x -axis direction, 3.82 in the y -axis direction, and 1.85 in the z -axis direction.

Aerodynamic Power

Figure 7 illustrates the aerodynamic power of the FOWT for the two different inflow wind conditions. It is expected that the oscillation feature of the aerodynamic power is observed for both inflow wind conditions as a result of the platform motions induced by the incident wave. For the atmospheric inflow, the varying amplitude is slightly greater than that of the uniform inflow, which can be attributed to the instability of wind speed of atmospheric inflow. However, the enhanced varying amplitude is very limited as a result of the active controllers—that is, the variable-torque controller for improved aerodynamic power and the blade-pitch controller for reduced aerodynamic power. To present more details about the aerodynamic power, a narrow time range of the aerodynamic power is presented in Fig. 7b. For the uniform inflow, the rotor power presents a periodic variation, in which the bigger and smaller periods correspond to the incident wave period

Case	Inflow wind		Incident wave		
	Type	Wind velocity	Type	Wave height	Wave period
Atmospheric Uniform	NBL inflow Uniform inflow	11.4 m/s	Stokes first-order deep water wave	7.58 m	12.1 s

Table 3 Inflow conditions for the FOWT

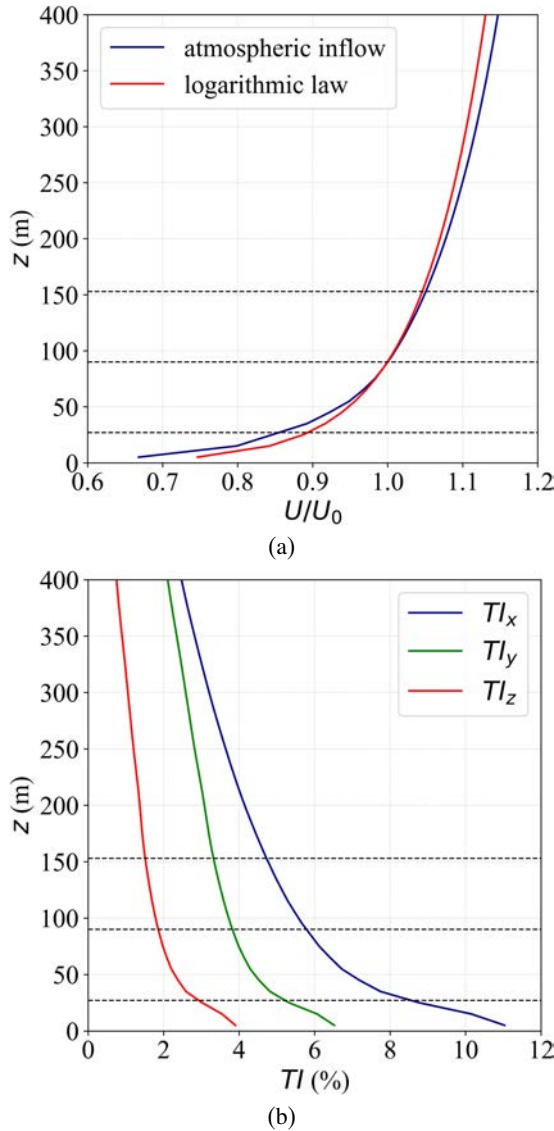


Fig. 6 Statistical characteristics of the simulated atmospheric inflow: (a) wind velocity profile and (b) turbulence intensity in three directions; the three black dotted lines denote the heights of the blade top, hub, and blade bottom

and the blade rotation period, respectively. Similar to the uniform wind condition, the periodic variation is also evident in the atmospheric scenario. However, small bumps caused by small-scale atmospheric turbulence structures can also be observed.

The statistics of the aerodynamic power of the FOWT for the two inflow wind conditions are shown in Table 4, which includes the values of the maximum, mean, minimum, root mean square (Rms), and standard deviation (Std). Although the varying amplitude of the aerodynamic power for the atmospheric inflow is slightly more enhanced than that of the uniform inflow, the mean values of the aerodynamic power for the atmospheric and uni-

Case	Aerodynamic power (MW)				
	Max	Mean	Min	Rms	Std
Atmospheric	6.70	5.27	4.01	5.29	0.47
Uniform	6.20	5.34	4.52	5.36	0.42

Table 4 Statistics of the aerodynamic power of the FOWT for the two inflow wind conditions

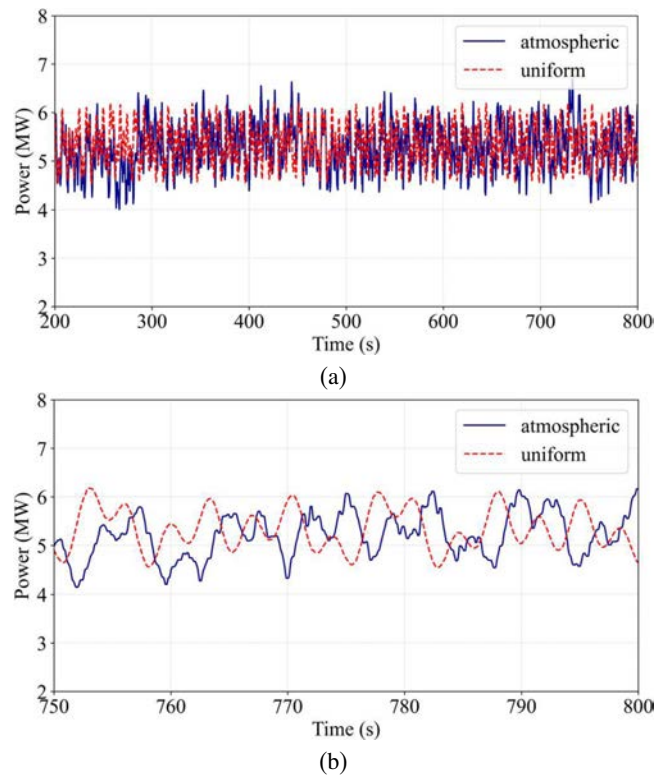


Fig. 7 Aerodynamic power of the FOWT for the two inflow wind conditions: (a) time range of 200–800 s and (b) time range of 750–800 s

form inflow scenarios are 5.27 MW and 5.34 MW, respectively, indicating a minor distinction. Besides this, the standard deviation of the aerodynamic power is also slightly more enhanced in the atmospheric scenario.

Yaw Moment

Different from the aerodynamic power, a significant distinction of the yaw moment for the two inflow scenarios is observed, as illustrated in Fig. 8. For the uniform inflow, the periodic variation of the yaw moment with minor varying amplitude is evident as a result of the incident regular wave. However, the varying amplitude is significantly increased in the atmospheric scenario, which can be attributed to the lateral asymmetry of the atmospheric inflow on the rotor plane. In addition to the periodic variation of the yaw moment induced by the incident wave, an insufficient

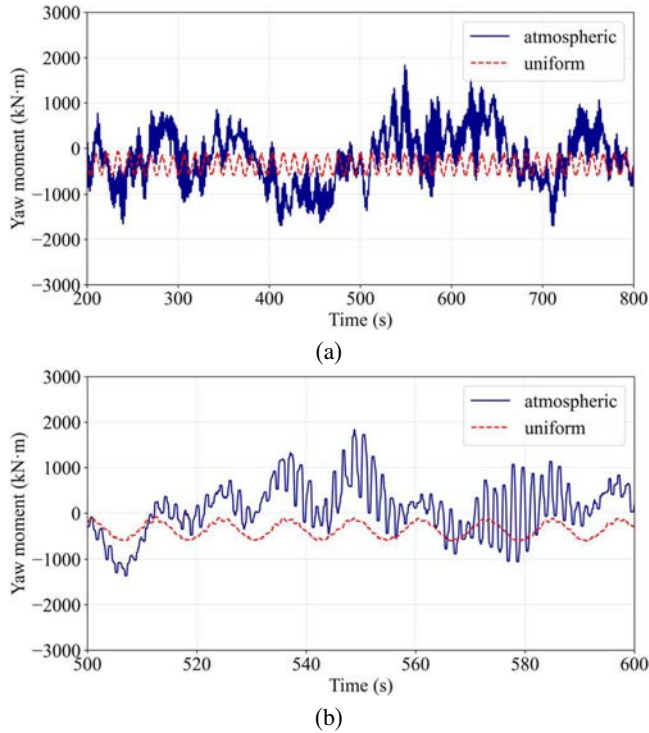


Fig. 8 Yaw moment of the FOWT for the two inflow wind conditions: (a) time range of 200–800 s and (b) time range of 500–600 s

Case	Yaw moment (kN · m)				
	Max	Mean	Min	Rms	Std
Atmospheric	1,835.0	−193.2	−1,698.0	629.1	598.8
Uniform	−61.1	−366.2	−609.1	398.8	158.0

Table 5 Statistics of the yaw moment of the FOWT for the two inflow wind conditions

periodic variation caused by the blade passage under the uniform inflow is observed if we take a closer look at Fig. 8b. The periodic variation of the yaw moment as a result of the blade passage is more visible in the atmospheric scenario.

Table 5 presents the statistics of the yaw moment in the two inflow scenarios. Undoubtedly, the standard derivation of the yaw moment in the atmospheric scenario is increased, owing to the significantly increased varying amplitude, which is 3.8 times that of the uniform inflow. In addition, the root mean square of the yaw moment is enhanced by the atmospheric inflow approximately 1.6 times that of the uniform scenario. Consequently, more efforts of fatigue loads of the yaw control system are required when compared with the FOWT subjected to the atmospheric inflow.

Platform Motions

Figure 9 presents the six degrees-of-freedom motions of the floating platform under the two inflow wind conditions. There is almost no difference for the platform heave motion because of the small vertical component of aerodynamic force compared with the platform wave force. For the platform sway and roll motions, a similar conclusion can also be obtained, but the small oscillations are presented in the atmospheric inflow. Minor distinctions in platform surge motion and pitch motion in the two inflow scenarios are observed. Furthermore, the platform pitch motion under the atmospheric inflow exhibits a relatively unstable varying characteristic, which is probably caused by the unstable aerodynamic

thrust exerted on the wind turbine. A difference in the platform yaw motion between the two inflow wind conditions is observed. The oscillation amplitude of the platform yaw motion is over 2° in the atmospheric scenario, significantly larger than that of the uniform inflow, which is induced by the significantly different yaw moment as mentioned before. Overall, the difference in the floating platform motions between the two inflow conditions is not distinct because of the large mass and inertia of the OC4 floating platform (Robertson et al., 2014).

Instantaneous Velocity Contours

Figure 10 shows the instantaneous velocity contours of the hub height plane for the two inflow wind conditions. Compared with the uniform inflow, the complex characteristics of the atmospheric inflow on the turbine rotor are clearly observed; these characteristics are responsible for the significant yaw moment. With respect to the uniform scenario, the minor wake meandering appears at a downstream distance of $3D$ (D is the rotor diameter), and the wake breaking is visualized at a downstream distance of $4D$. The presence of a complex atmospheric inflow allows us to clearly observe the wake meandering at a downstream distance of $1D$. Besides this, the magnitude of the wake meandering is significantly increased with streamwise distance, as represented by the black dotted lines. The wake breaking is accelerated (approximately at a downstream distance of $2D$) because of the more unstable wake shear layer in the atmospheric scenario compared with that of the uniform scenario, and the wake is completely broken down at the downstream distance of $4D$.

Figure 11 shows the instantaneous velocity contours of the vertical plane through the rotor center for the two inflow wind conditions. The wake in the uniform scenario is discovered to deflect upward, induced by the platform pitch motion. A pair of low-velocity air masses are observed periodically shedding from the near wake. For the atmospheric scenario, from the sea surface to the hub height, a large-scale low-velocity airflow is widely distributed, which is possibly responsible for the significant difference in the aerodynamic pitch moment compared with that in the uniform scenario. With increasing downstream distance, the lower wake velocity below the hub height deflects to the hub height. In addition, the high-velocity atmospheric airflow enters in the wind turbine wake, and its mixing with the low-velocity wake leads to a faster wake velocity recovery.

Vortical Structures

Figure 12 illustrates the vortical structures for the two inflow wind conditions. When the inflow wind passes through the wind turbine, the helical blade-tip vortices are induced by the wind turbine. The blade-tip vortices quickly break with increasing travel distance, and the finer vortices are visualized in the far wind turbine wakes. Compared with the uniform inflow scenario, some vortical structures upstream of the wind turbine are evident for the atmospheric inflow case. Owing to the ambient vortices and their interactions with the vortices induced by the wind turbine, large-scale vortices, as well as more sophisticated and finer vortices, in wind turbine wakes can be observed, and wake meandering is visible.

CONCLUSIONS

In this study, numerical investigations of the FOWT were performed considering two different inflow wind conditions (atmospheric and uniform inflows), in which an NREL 5MW reference wind turbine mounted on the OC4 semisubmersible floating

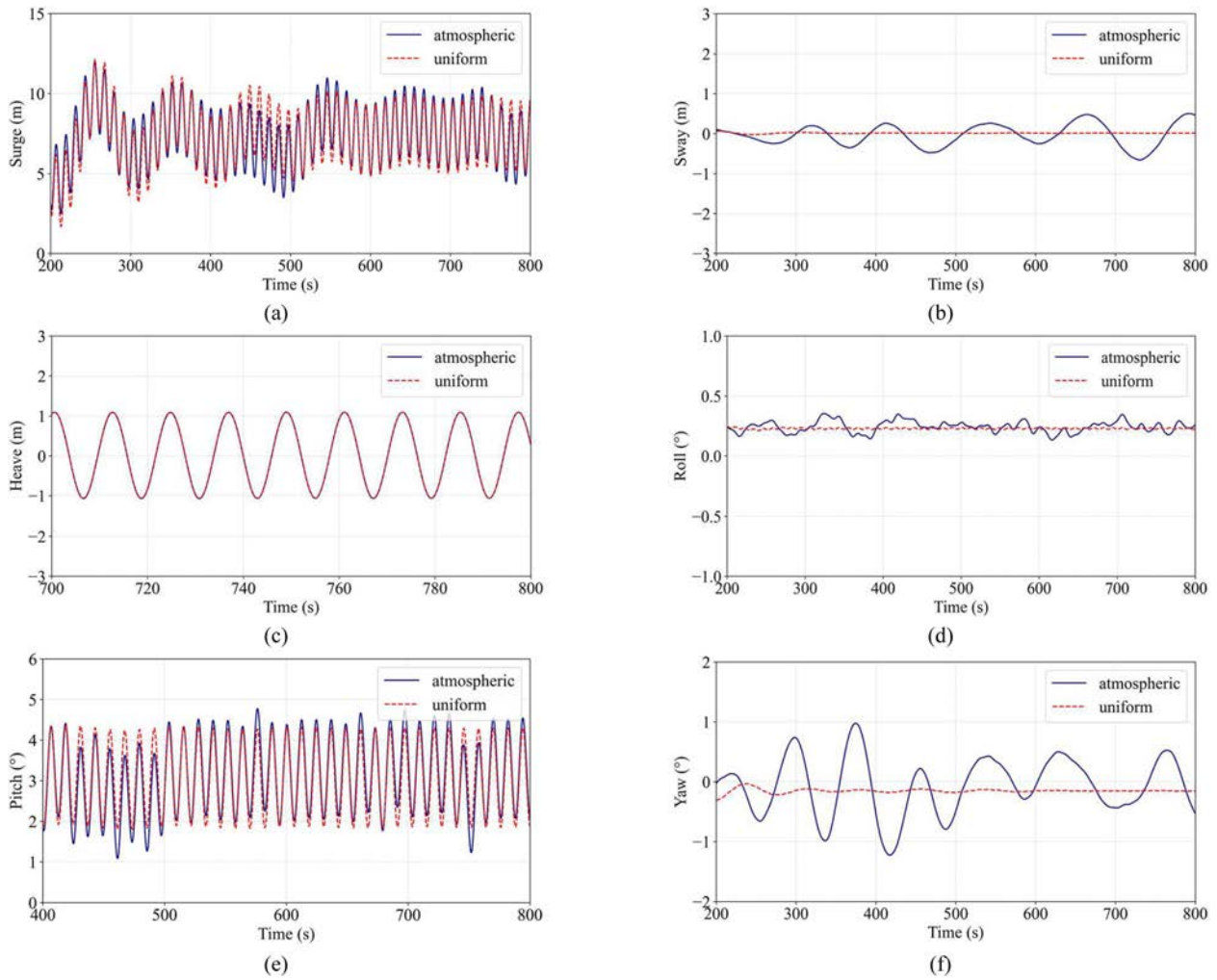


Fig. 9 Floating platform motions for the two inflow wind conditions: (a) surge, (b) sway, (c) heave, (d) roll, (e) pitch, and (f) yaw

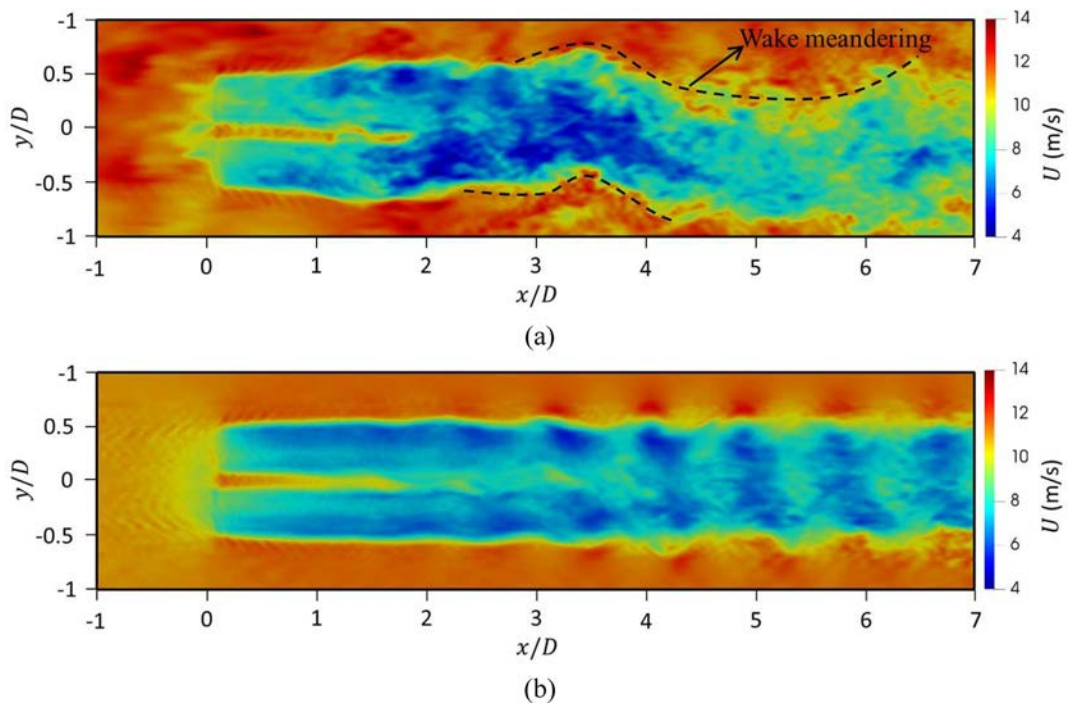


Fig. 10 Instantaneous velocity contours of the hub height plane for the two inflow wind conditions: (a) atmospheric scenario and (b) uniform scenario

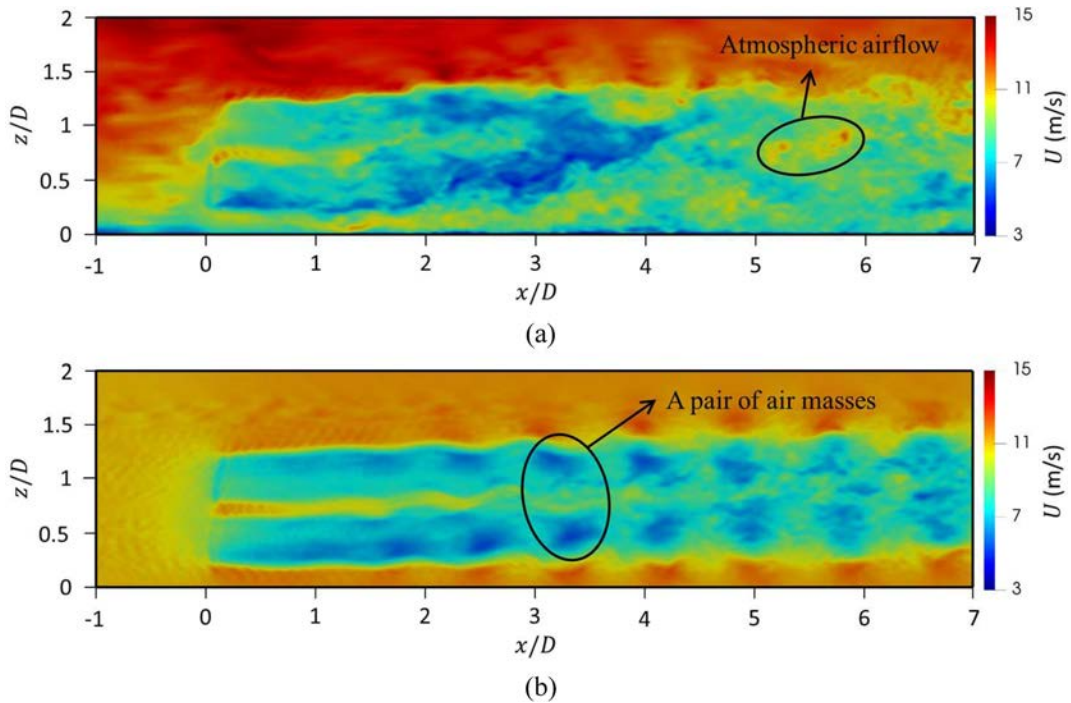


Fig. 11 Instantaneous velocity contours of the vertical plane through the rotor center for the two inflow wind conditions: (a) atmospheric scenario and (b) uniform scenario

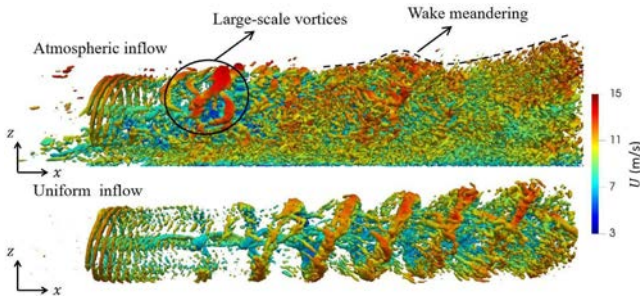


Fig. 12 The vortical structures for the two inflow scenarios

platform was employed as the research object. According to the analysis of aerodynamic power, yaw moment, floating platform motions, and wake velocity fields, the following conclusions can be drawn.

The difference in the aerodynamic power of the two inflow scenarios is minor, except that small bumps of aerodynamic power in the atmospheric scenario caused by small-scale turbulence structures are observed. However, the yaw moment is significantly enhanced as a result of the lateral asymmetry of the atmospheric inflow on the rotor plane, leading to an increase of its standard derivation to 3.8 times that of the uniform inflow. The difference in the floating platform yaw motion in the two inflow scenarios is subsequently observed. The oscillating amplitude for the atmospheric inflow is over 2° , whereas the output value for the uniform inflow is steady and does not exceed 0.2° . In addition, some minor distinctions of the surge and pitch motions for the two inflow conditions are observed.

As for the instantaneous velocity contours, complex characteristics of the atmospheric inflow on the turbine rotor plane are clearly observed. For the contours of the hub height plane, a significant observation is made for the large-scale wake meandering as a result of the presence of atmospheric turbulence structures. The downstream distance of the wake breaking is decreased as a result of the more unstable wake shear layer in the atmospheric

scenario. With respect to the vertical plane through the rotor center, the wake in the uniform scenario is discovered to deflect upward as a result of the platform pitch motion, and a pair of low-velocity air masses are observed periodically shedding from the near wake. In the atmospheric inflow scenario, the high-velocity atmospheric airflow enters in the wind turbine wake, and its mixing with the low-velocity wake leads to a faster recovery of the wake. Furthermore, because of the vortices of atmospheric inflow and their interactions with the wind turbine vortices, the large-scale vortices, as well as more sophisticated and finer vortices, in wind turbine wakes can be observed, and wake meandering is visible.

ACKNOWLEDGEMENTS

This work was supported by the National Natural Science Foundation of China (Grant No. 52131102) and the Key Laboratory of Far-Shore Wind Power Technology of Zhejiang Province, to which the authors are most grateful.

REFERENCES

- Asim, T, Islam, SZ, Hemmati, A, and Khalid, MSU (2022). "A Review of Recent Advancements in Offshore Wind Turbine Technology," *Energies*, 15(2), Article 579. <https://doi.org/10.3390/en15020579>.
- Chanprasert, W, Sharma, RN, Cater, JE, and Norris, SE (2022). "Large Eddy Simulation of Wind Turbine Fatigue Loading and Yaw Dynamics Induced by Wake Turbulence," *Renewable Energy*, 190, 208–222. <https://doi.org/10.1016/j.renene.2022.03.097>.
- Chehouri, A, Younes, R, Ilinca, A, and Perron, J (2015). "Review of Performance Optimization Techniques Applied to Wind Turbines," *Appl Energy*, 142, 361–388. <https://doi.org/10.1016/j.apenergy.2014.12.043>.

- Cheng, P, Huang, Y, and Wan, D (2019). “A Numerical Model for Fully Coupled Aero-hydrodynamic Analysis of Floating Offshore Wind Turbine,” *Ocean Eng*, 173, 183–196. <https://doi.org/10.1016/j.oceaneng.2018.12.021>.
- Churchfield, MJ, Lee, S, Michalakes, J, and Moriarty, PJ (2012). “A Numerical Study of the Effects of Atmospheric and Wake Turbulence on Wind Turbine Dynamics,” *J Turbul*, 13, N14. <https://doi.org/10.1080/14685248.2012.668191>.
- Churchfield, M, Lee, S, and Moriarty, P (2012). *Overview of the Simulator for Wind Farm Application (SOWFA)*, Report, National Renewable Energy Laboratory, Golden, CO, USA, 96 pp.
- Global Wind Energy Council (2021). *Global Wind Report 2021*, Report, Global Wind Energy Council.
- Huang, Y, Cheng, P, and Wan, D (2019). “Numerical Analysis of a Floating Offshore Wind Turbine by Coupled Aero-hydrodynamic Simulation,” *J Mar Sci Appl*, 18(1), 82–92. <https://doi.org/10.1007/s11804-019-00084-8>.
- Huang, Y, and Wan, D (2019). “Investigation of Interference Effects Between Wind Turbine and Spar-type Floating Platform under Combined Wind-wave Excitation,” *Sustainability*, 12(1), Article 246. <https://doi.org/10.3390/su12010246>.
- Johlas, H (2021). *Simulating the Effects of Floating Platforms, Tilted Rotors, and Breaking Waves for Offshore Wind Turbines*, PhD thesis, University of Massachusetts, Amherst, MA, USA, 187 pp.
- Johlas, HM, Martínez-Tossas, LA, Lackner, MA, Schmidt, DP, and Churchfield, MJ (2020). “Large Eddy Simulations of Offshore Wind Turbine Wakes for Two Floating Platform Types,” *J Phys Conf Ser*, 1452(1), Article 012034. <https://doi.org/10.1088/1742-6596/1452/1/012034>.
- Johlas, HM, Martínez-Tossas, LA, Schmidt, DP, Lackner, MA, and Churchfield, MJ (2019). “Large Eddy Simulations of Floating Offshore Wind Turbine Wakes with Coupled Platform Motion,” *J Phys Conf Ser*, 1256(1), Article 012018. <https://doi.org/10.1088/1742-6596/1256/1/012018>.
- Jonkman, JM, and Buhl, ML (2005). *FAST User’s Guide*, Report NREL/TP-500-38230, National Renewable Energy Laboratory, Golden, CO, USA.
- Jonkman, J, Butterfield, S, Musial, W, and Scott, G (2009). *Definition of a 5-MW Reference Wind Turbine for Offshore System Development*, Report NREL/TP-500-38060, National Renewable Energy Laboratory, Golden, CO, USA.
- Kaimal, JC, Wyngaard, J, Izumi, Y, and Coté, OR (1972). “Spectral Characteristics of Surface-layer Turbulence,” *Q J R Meteorolog Soc*, 98(417), 563–589. <https://doi.org/10.1002/qj.49709841707>.
- Lee, S, Churchfield, M, Moriarty, P, Jonkman, J, and Michalakes, J (2012). “Atmospheric and Wake Turbulence Impacts on Wind Turbine Fatigue Loadings,” *50th AIAA Aerosp Sci*, Nashville, TN, USA, American Institute of Aeronautics and Astronautics, AIAA-2012-0540. <https://doi.org/10.2514/6.2012-540>.
- Li, L, Liu, Y, Yuan, Z, and Gao, Y (2018). “Wind Field Effect on the Power Generation and Aerodynamic Performance of Offshore Floating Wind Turbines,” *Energy*, 157, 379–390. <https://doi.org/10.1016/j.energy.2018.05.183>.
- Li, T, Liu, Z, Wang, H, Bian, W, and Yang, Q (2022). “Large Eddy Simulation for the Effects of Ground Roughness and Atmospheric Stratification on the Wake Characteristics of Wind Turbines Mounted on Complex Terrains,” *Energy Convers Manage*, 268, 115977. <https://doi.org/10.1016/j.enconman.2022.115977>.
- Liu, X, et al. (2022). “Large-eddy Simulation of Wakes of Waked Wind Turbines,” *Energies*, 15(8), 2899. <https://doi.org/10.3390/en15082899>.
- Moeng, C-H (1984). “A Large-eddy-simulation Model for the Study of Planetary Boundary-layer Turbulence,” *J Atmos Sci*, 41(13), 2052–2062. [https://doi.org/10.1175/1520-0469\(1984\)041<2052:ALESMF>2.0.CO;2](https://doi.org/10.1175/1520-0469(1984)041<2052:ALESMF>2.0.CO;2).
- Mann, J (1994). “The Spatial Structure of Neutral Atmospheric Surface-layer Turbulence,” *J Fluid Mech*, 273, 141–168. <https://doi.org/10.1017/S0022112094001886>.
- Ning, X, and Wan, D (2019). “LES Study of Wake Meandering in Different Atmospheric Stabilities and Its Effects on Wind Turbine Aerodynamics,” *Sustainability*, 11(24), 6939. <https://doi.org/10.3390/su11246939>.
- Nybø, A, Nielsen, FG, and Godvik, M (2022). “Sensitivity of the Dynamic Response of a Multimegawatt Floating Wind Turbine to the Choice of Turbulence Model,” *Wind Energy*, 25(6), 1013–1029. <https://doi.org/10.1002/we.2712>.
- OpenFOAM Foundation (2022). *OpenFOAM and the OpenFOAM Foundation*, <https://openfoam.org/> (Accessed September 22, 2022).
- Robertson, A, et al. (2014). *Definition of the Semisubmersible Floating System for Phase II of OC4*, Report NREL/TP-5000-60601, National Renewable Energy Laboratory, Golden, CO, USA.
- Smagorinsky, J (1963). “General Circulation Experiments with the Primitive Equations: I. The Basic Experiment,” *Mon Weather Rev*, 91(3), 99–164. [https://doi.org/10.1175/1520-0493\(1963\)091<0099:GCEWTP>2.3.CO;2](https://doi.org/10.1175/1520-0493(1963)091<0099:GCEWTP>2.3.CO;2).
- Sorensen, JN, and Shen, WZ (2002). “Numerical Modeling of Wind Turbine Wakes,” *J Fluids Eng*, 124(2), 393–399. <https://doi.org/10.1115/1.1471361>.
- Troldborg, N (2009). *Actuator Line Modeling of Wind Turbine Wakes*, PhD thesis, Technical University of Denmark, 142 pp.
- Zhou, Y, et al. (2022). “Exploring Inflow Wind Condition on Floating Offshore Wind Turbine Aerodynamic Characterisation and Platform Motion Prediction Using Blade Resolved CFD Simulation,” *Renewable Energy*, 182, 1060–1079. <https://doi.org/10.1016/j.renene.2021.11.010>.